Optical studies of ballistic currents in semiconductors [Invited]

Brian A. Ruzicka and Hui Zhao*

Department of Physics and Astronomy, The University of Kansas, Lawrence, Kansas 66045, USA
**Corresponding author: huizhao@ku.edu*

Received October 17, 2011; accepted November 23, 2011;
posted November 29, 2011 (Doc. ID 156678); published January 25, 2012

We present a summary of recent studies of ballistic currents using nonlinear optical techniques. Quantum interference between one- and two-photon absorption pathways is used to inject and control ballistic currents in GaAs samples. With this, a pure charge current, pure spin current, or spin-polarized charge current can be injected by changing the polarization configuration of the two pump pulses. Such currents are temporally and spatially resolved using high-resolution pump–probe techniques, including a derivative-detection scheme, which allows detection of the motion of carriers as small as 0.1 nm. Observation of the intrinsic inverse spin Hall effect in the ballistic regime, a study of time-resolved ballistic spin-polarized charge currents, and a study of the efficiency of spin current injection by quantum interference were all achieved using these techniques. Additionally, we discuss demonstrations of second-order nonlinear optical effects induced by charge and spin currents, which allow for the nondestructive, noninvasive, and real-time imaging of currents.

OCIS codes: 320.7130, 190.5970, 320.7110.

1. INTRODUCTION

Charge carrier transport in semiconductors is the foundation of the modern semiconductor industry. It has been extensively investigated for several decades. However, most of these studies have been performed on carrier systems that are in thermal equilibrium with the lattice. In this regime, the transport can be described by the macroscopic quantities of mobility and the diffusion coefficient, which are straightforwardly related to microscopic quantities of the mean free path and mean free time. However, in a practical device, carriers are usually injected with a nonthermal distribution. It takes multiple carrier–carrier scattering events for the carriers to exchange energy in order to establish a thermal distribution and multiple carrier–phonon scattering events for the carrier system to reach a thermal equilibrium with the lattice. Under typical conditions, the mean free length of the carriers is on the order of 10 to 100 nm [1]. Hence, equilibrium carrier transport can only be established on larger length scales. However, feature sizes of electronic devices in integrated circuits have already been reduced to 60 nm, and they will approach 20 nm soon. Because the device dimensions are comparable to or even smaller than the mean free path, carriers can move through the device with few or even no collisions. Therefore, there is no room for the carriers to reach thermal equilibrium with the lattice, and the nonthermal, nonequilibrium carrier transport plays a dominant role in nanoscale devices.

Studies of nonequilibrium carrier nanoscale transport require experimental techniques with a high temporal resolution because the transport occurs on ultrafast time scales of at most a few picoseconds. Electrical detection techniques that are generally used in transport studies have limited temporal resolution. Ultrafast laser techniques are standard tools to study nonequilibrium carrier dynamics in semiconductors, owing to their superior temporal resolution [2]. Several laser techniques to study carrier transport have been developed, including the transient grating [3–8], spatially resolved pump–probe [9–20], and spatially resolved photoluminescence [21–26]. However, the spatial resolution of these techniques is limited to the order of the wavelength of the light. This imposes severe constraints on studies of nonequilibrium carrier transport, which occurs on much shorter length scales.

It has also been widely recognized that the future of electronic technology relies on revolutionary development because the current technology is approaching the fundamental limit on device size. One promising candidate is spintronics, in which the spin of electrons is used in addition to, or in place of, charge [27–29]. Considering spin as well as charge, carrier transport can lead to three different types of currents. In conventional devices, carriers have random spin orientations. Transport of such a spin-unpolarized carrier system leads to a pure charge current, without a spin current. In contrast, movement of a spin-polarized carrier system produces both a charge and a spin current. This is often called a spin-polarized charge current. Finally, it is possible to generate a pure spin current, with no charge current. In this type of current, equal numbers of carriers with opposite spin orientations move oppositely. Because the charge currents carried by the two spin systems cancel, there is no net charge current. However, the spin currents by the two spin systems superimpose, resulting in a pure spin current.

Because spin transport in semiconductors plays a key role in spintronics, over the past ten years several optical techniques have been developed to study spin transport in semiconductors. For example, by measuring polarization properties of photoluminescence, spin transport in GaAs bulk [30,31] and quantum wires [32] has been studied. Spin transport carried by surface acoustic waves has also been demonstrated with this method [33–35]. Another extensively used optical technique is based on rotation of linear polarization of light by the effective magnetic field of spin-polarized electrons. The Faraday (transmission geometry) and Kerr (reflection geometry)

rotation techniques have been applied in studies of transport of spins injected by optical orientation [36–39], the spin Hall effect [40–44], and from ferromagnets [45]. Very recently, a spin transient-grating technique was successfully used in studies of the spin Coulomb drag effect [46], spin diffusion [47], and persistent spin helix [48,49]. However, as in the studies of charge transport, the limited spatial resolution of these techniques confined them to study only equilibrium spin transport over large length scales.

In this article, we will review our recent studies of ballistic charge and spin transport using optical techniques that are not constrained by the conventional spatial resolution of optical systems set by the diffraction limit. We will first introduce some fundamentals of optical injection of ballistic currents by utilizing quantum interference between multiple absorption pathways. The first optical technique we used to study the ballistic currents is based on a pump-probe technique with a derivative-detection scheme. In this scheme, the smallest detectable motion is determined by the signal-to-noise ratio (SNR) instead of the laser spot size. We will describe three recent experiments using this scheme: the intrinsic inverse spin Hall effect, dynamics of ballistic spin-polarized charge currents, and efficiency of current injection by quantum interference. The second technique uses second-order nonlinear optical effects induced by the currents. This technique directly senses the velocity of the carriers. Hence, it is not necessary to spatially resolve the position of the carriers during their nanoscale transport. We will discuss our demonstrations of the second-harmonic generation induced by pure spin currents and pure charge currents.

2. OPTICAL INJECTION OF BALLISTIC CURRENTS

In a typical transport measurement, carriers are driven by an externally applied electric field. An acceleration process is required to establish an equilibrium current. Because the acceleration time is much longer than the thermalization time, the transport is in the drift-diffusion regime. On the other hand, interband excitation by ultrafast laser pulses can instantaneously inject nonequilibrium carriers, but because the excitation is symmetric in crystal-momentum space (k space), equal numbers of carriers are injected with opposite average velocities along any direction, and no macroscopic current exists.

However, in the early 1990s, it was proposed and demonstrated that quantum interference between multiple absorption pathways can be used to inject ballistic currents. Although the first demonstration used transitions from impurity levels to the conduction band driven by infrared pulses [50], most studies involve interband transitions [51–72]. The key element for breaking the k-space symmetry of the optical excitation is that the transition amplitude of two-photon absorption, A_2, is approximately an odd function of k. Although the transition probability of two-photon absorption $P_2 = |A_2|^2$ is still an even function of k, it is possible to interfere this process with another one with an even transition amplitude, so that the interference terms are odd. One obvious choice is one-photon absorption between the same two states, with an amplitude $A_1(k) = A_1(-k)$. If the two transition pathways are present simultaneously, the overall transition probability is

$$P = |A_1 + A_2|^2 = |A_1|^2 + |A_2|^2 + A_1A_2^* + A_1^*A_2. \quad (1)$$

The first two terms on the right-hand side of Eq. 1 are the transition probabilities of one- and two-photon absorption when existing alone. They are both even functions of k and hence do not contribute to a current. The other two terms are the interference terms, and are odd functions of k. Therefore, in most cases, $P(k) \neq P(-k)$.

Figure 1 illustrates three configurations used to inject different types of ballistic currents in semiconductors. In the first configuration [Fig. 1(a)], the semiconductor sample is simultaneously illuminated by two phase-locked laser pulses with angular frequencies ω and 2ω [red and green waves in Fig. 1(a)] that are both linearly polarized along an arbitrarily chosen $\hat{x}$ direction. When $\hbar\omega < E_g < 2\hbar\omega$, where E_g is the bandgap of the sample, the ω (2ω) pulse drives the two (one)-photon absorption. By choosing a proper relative phase between the two pulses, we can arrange the two amplitudes to interfere constructively at states with positive k values, and destructively at states with negative k values. The average velocity of the excited electrons is $\eta_c v \sin(\Delta\phi)\hat{x}$, where v is the speed of each electron determined by the excitation

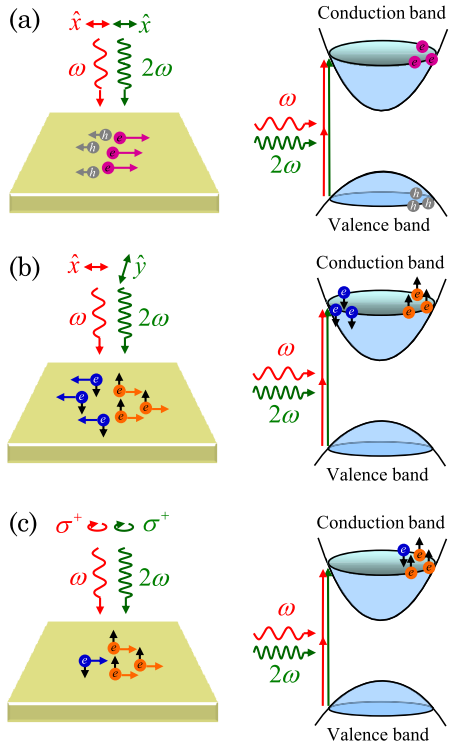

Fig. 1. (Color online) QUIC technique to inject ballistic currents. (a) Two $\hat{x}$-polarized laser pulses with angular frequencies of ω and 2ω inject electrons (e) and holes (h) into the conduction and the valence bands by simultaneous two-photon absorption of the ω pulse and one-photon absorption of the 2ω pulse. Electrons are excited with an average velocity along the $\hat{x}$ direction as a result of the quantum interference between the two transition amplitudes. Holes are injected with an average velocity along the opposite direction. (b) The $\hat{x}$-polarized ω pulse and $\hat{y}$-polarized 2ω pulse excite spin-up electrons with an average velocity along $\hat{x}$, with an equal number of spin-down electrons with opposite average velocity. Hence, a pure spin current along $\hat{x}$ is injected. (c) Two circularly polarized pulses excite spin-polarized electrons with an average velocity along a direction that is determined by the relative phase of the two pulses. A spin-polarized charge current is injected. In panels (b) and (c), the holes are not plotted for clarity.

excess energy and $\Delta\phi = 2\phi_\omega - \phi_{2\omega}$ is determined by the phases of the two pulses. The η_c is a parameter describing the efficiency of interference, and it is typically on the order of 0.1 [57]. Hence, a charge current is injected along $\hat{x}$. Owing to the crystal momentum conservation, holes are injected in the valence band with an opposite crystal momentum. The charge current carried by the holes is along the same direction as the electronic current, but it is usually weaker because, in most materials, the holes have larger effective masses than the electrons in the conduction band. However, the holes can play an important role in determining the dynamics of the currents.

In this scheme, carriers are instantaneously injected to high-energy states by ultrafast laser pulses, and therefore no acceleration process is required—the carriers start their motion with a high speed. Because it takes time for the moving carriers to undergo collisions with themselves and phonons, these instantaneously injected currents are known as ballistic currents. Therefore, the quantum interference and control (QUIC) technique is a powerful tool to study ballistic transport.

Injection of ballistic pure charge current by the QUIC technique, as illustrated in Fig. 1(a), was originally proposed in 1996 [51,73]. It was soon demonstrated experimentally in GaAs by observing steady-state charge accumulation [52,74]. It was also demonstrated that the injected ballistic charge current can be studied by detecting the electromagnetic radiation by the current, with frequencies in the THz range [55], or by a spatially resolved pump–probe technique [56]. Additionally, it was used to stabilize the carrier–envelope phase of femtosecond lasers [53,54,75,76]. More recently, injection of pure charge currents by the QUIC technique in other materials and structures has been achieved, including GaAs quantum wells [56], silicon [70,71], germanium [70], CdSe and CdTe [69], carbon nanotubes [72,77], graphite [72,77], and graphene [78]. Other variations of the QUIC technique have also been demonstrated. For example, it was shown that the two-photon absorption can be nondegenerate (i.e., absorption of two photons with different energies, with the sum equal to the one-photon transition energy) [79]. As another example, when the two excitation beams are not collinearly incident to the sample, a charge current grating can be injected [80,81]. These experimental studies were also accompanied by extensive theoretical efforts [82–85].

Figure 1(b) shows the configuration used to inject pure spin currents. When the ω pulse is still linearly polarized along the $\hat{x}$ direction but the 2ω pulse is linearly polarized along the perpendicular $\hat{y}$ direction, spin-up electrons are preferentially injected to the conduction band states with positive k values, with the same density of the spin-down electrons to the states with negative k values. The average velocities of the two spin systems are opposite, $\langle \rightarrow v\rangle^{\uparrow} = -\langle \rightarrow v\rangle^{\downarrow} = \eta_s v \cos(\Delta\phi)\hat{x}$. Because there are equal number of electrons moving with opposite average velocities, there is no net electron transport and no net charge current. However, the spin currents carried by the two spin systems add together, resulting in a pure spin current along the $+\hat{x}$ direction.

Injection of pure spin current by the QUIC technique was originally proposed in 2000 [57] and has been demonstrated experimentally in GaAs [58,86] ZnSe [59], and Ge [87] by using a spatially resolved pump–probe technique [58,87], transient-grating technique [86], and photoluminescence [59]. Compared to other available techniques to generate pure spin currents [40,88–94], the QUIC technique has two significant advantages: the current injected is ballistic and the current density can be very high.

Finally, the QUIC technique can be used to inject ballistic spin-polarized charge currents, as illustrated in Fig. 1(c). Here, the two pulses are both circularly polarized with the same sign (for example σ^+). Because of spin-selection rules, spin-polarized electrons are injected to the conduction band. With the quantum interference, these electrons are excited with a nonzero average velocity $\eta_{sc} v[\cos(\Delta\phi)\hat{x} + \sin(\Delta\phi)\hat{y}]$, where η_{sc} describes the current injection efficiency. Hence, in this configuration the $\Delta\phi$ controls the direction, instead of the magnitude, of the injected current. Following the initial theoretical proposal [57], injection of spin-polarized charge current by the QUIC technique was also demonstrated experimentally [95].

3. HIGH-RESOLUTION PUMP–PROBE STUDIES OF BALLISTIC CURRENTS

A. Derivative Detection

Because of the diffraction of light, the spatial resolution of a far-field optical system is limited to the order of micrometers. This is the main obstacle in studies of nanoscale ballistic transport by optical techniques. In order to achieve high spatial resolution, a derivative-detection scheme was developed, and it was first used to detect pure spin currents [58].

The principle of the derivative-detection scheme is rather simple, as illustrated in Fig. 2. Initially, carriers are excited to a Gaussian spatial density profile of width W (full-width at half-maximum, FWHM) and height H [solid Gaussian curve in Fig. 2(a), $N(0)$] by tightly focused laser pulses. If the carriers are injected with an average velocity along $\hat{x}$, the profile moves along $\hat{x}$. After a short period of time of τ, the profile is shifted by a distance of d, to a new position [dotted Gaussian curve, $N(\tau)$]. For ballistic transport, $d \ll W$. Therefore, a direct-imaging method with a spatial resolution of about W cannot be used to measure d.

To solve this resolution problem, the difference between the final and initial profiles, $\Delta N = N(\tau) - N(0)$, is directly

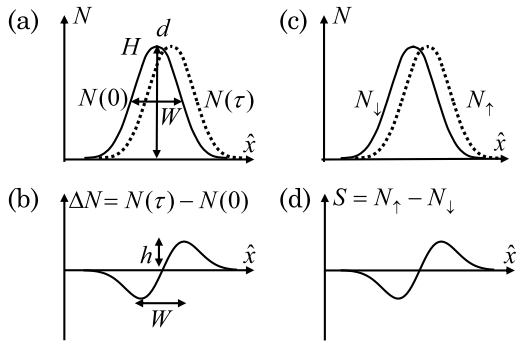

Fig. 2. Derivative-detection scheme to spatially resolve ballistic charge [(a), (b)] and spin [(c), (d)] currents. In a charge current, electrons with a Gaussian spatial profile [$N(0)$, solid line in (a)] of width W and height H are injected with an average velocity along $\hat{x}$. After a short period of time, τ, the profile has moved a distance d to a new position [$N(\tau)$, dashed line]. The difference of the two profiles [ΔN, solid line in (b)] has a derivativelike profile with spatial features on the order of W and hence can be spatially resolved. From ΔN, W, and H, one can deduce d. When a pure spin current is injected, spin-up [dashed line in (c)] and spin-down (solid line) electrons separate, resulting in a derivativelike spin density profile [S, solid line in (d)].

measured. This is done by introducing modulations between the two profiles and detecting the signal by a lock-in amplifier. This ΔN, which can be viewed as the change of the carrier density due to the transport, has a derivativelike spatial profile, as shown as the solid line in Fig. 2(b). The amplitude of this profile, h, is proportional to d. Because the two peaks of the ΔN profile are separated by a distance W, the profile can be spatially resolved. Additionally, the sign of the derivativelike profile shows the direction of current flow. By measuring h as a function of time, we can deduce the time evolution of d by using the relation

$$\frac{d}{W} = 0.707\frac{h}{H}. \tag{2}$$

The same approach can be used to study a ballistic pure spin current. In a pure spin current, the two spin systems move oppositely, and hence they separate after a certain period of time, as shown in Fig. 2(c). The resulting spin density, defined as $S = N^{\uparrow} - N^{\downarrow}$, has a derivativelike profile, as shown in Fig. 2(d). The magnitude of this profile is related to the separation of the two spin profiles in the same way as Eq. (2). The sign of this profile is determined by the direction of the spin transport.

Hence, ballistic charge and spin transport over a distance that is much smaller than the laser spot can be accurately measured. Equation (2) also shows that the derivative-detection scheme converts a spatial resolution problem to an SNR problem: the left-hand side shows the distance to be measured (d) with respect to the spatial resolution (W), while the right-hand side shows the signal to be detected in this derivative-detection scheme (h) compared to the signal measured in a direct measurement (H). Therefore, to implement the derivative-detection scheme, it is necessary to reduce W by tightly focusing the laser pulses, modulate the two profiles, and increase the SNR.

B. Experimental Setup

Figure 3 shows the experimental setup used to inject ballistic charge and spin currents by the QUIC technique and spatially and temporally resolve the current dynamics. We use a diode-pumped solid-state laser to pump a Ti:sapphire laser that produces tunable infrared laser pulses of 100 fs duration with a repetition rate of 80 MHz. This output is used to pump an optical parametric oscillator (OPO) to generate 100 fs pulses around 1500 nm, serving as the ω pulse that drives the two-photon absorption in the QUIC technique. The 2ω pulse is

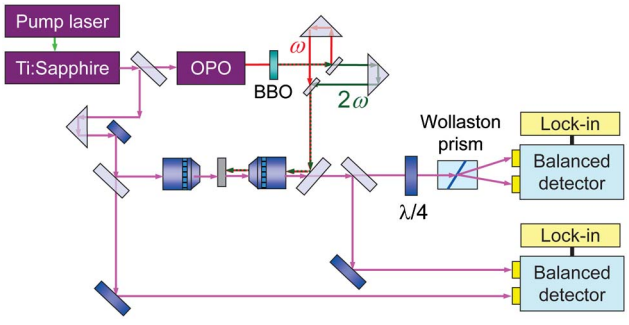

Fig. 3. (Color online) Experiment setup to inject ballistic charge and spin currents by the QUIC technique and spatially and temporally resolve the current dynamics.

obtained by second-harmonic generation (SHG) in a beta barium borate (BBO) crystal. The two pulses are sent through an interferometer in order to independently control their phase and polarizations, and then they are combined together and focused on the sample through a microscope objective lens with a high numerical aperture. As discussed in Section 2, by choosing different polarization configurations of the two pulses, we can inject different types of ballistic currents.

The dynamics of these ballistic currents is studied by using the derivative-detection scheme, as described in Subsection 3.A. The carrier density and the spin density can be simultaneously detected by analyzing differential transmission and carrier-induced circular dichroism of a probe pulse. The linearly polarized probe pulse can be viewed as a superposition of two circular components, σ^+ and σ^-, of the same amount. When going through the sample, both components will have some absorption, or equivalently a linear transmission that is less than 1 (the ratio between the transmitted intensity and the incident intensity). When no carriers are present, this linear transmission has some value, T_0. When carriers are present, the absorption will be reduced because the carriers block some final states involved in the interband absorption. Hence, the transmission with carriers present, T, will be different from T_0. The relative change, $\Delta T/T_0 = (T - T_0)/T_0$, is defined as the differential transmission. In the low-density regime, the differential transmission is proportional to the carrier density.

If the carriers are spin polarized, owing to the spin-selection rules, the absorption coefficients for the two circular components of the probe are different. Therefore, the transmitted probe has two unequal circular components. It then becomes elliptically polarized with a certain ellipticity. This is known as a circular dichroism. In addition, the indices of refraction for the two circular components are different, owing to the presence of the spin-polarized carriers. Therefore, the two circular components have different phase shifts when propagating through the sample. This causes a rotation of the polarization, which is called Faraday rotation. Both the induced ellipticity and the rotation angle are proportional to the spin density, under typical conditions.

The implementation of the derivative-detection scheme is also shown in Fig. 3. We take a small portion of the Ti:sapphire laser beam and focus it to the sample from the back side by using a microscope objective lens with a high numerical aperture. The transmitted pulse is collimated by the pump-focusing lens. It contains information about the carrier density and spin density at the location of the probe spot and the time when the pulse arrived at the sample. A beam splitter is used to divide the probe beam into two parts for analyzing the carrier and the spin densities separately. In order to measure the carrier density, the reflected part is sent to a photodiode of a balanced detector. The other photodiode of the same balanced detector receives a part of the probe that was taken before entering the sample. By matching the power of the two beams, the intensity noise of the probe beam is evenly distributed on the two detectors, and hence it is canceled at the output voltage of the balanced detector, which is proportional to the difference in the powers received by the two photodiodes. This voltage is measured by a lock-in amplifier.

When measuring N, a chopper is used to modulate the power of the pump beams that reaches the sample and therefore

the density of carriers injected by the pump. Hence, the voltage on the lock-in amplifier is proportional to N. When measuring ΔN, an electro-optic modulator is used to modulate the phase of the 2ω pulse. Because the injected current density is determined by $\Delta\phi$, we are essentially modulating the injected current density between a certain value and zero, if we choose a proper waveform of the voltage applied to the modulator. With zero current density, the injected carriers have no directional movement and the carrier density profile remains unchanged at later time delays. Hence, the profile at a later time delay without current injection mimics the profile at the initial time of current injection. Therefore, the modulation between the two profiles at a certain time delay with and without current injection is equivalent to a modulation between the two profiles at the initial and later time delay with current injection. Under this modulation scheme, the voltage on the lock-in amplifier is proportional to ΔN. Note that because the thermal diffusion occurs to both profiles, with and without current injection, it does not influence the measurement. Additionally, the broadening of the profile due to the diffusion is negligible on the short time scales in which ballistic transport occurs.

The spin density is measured by analyzing the ellipticity of the probe, by using the portion of the transmitted probe that goes through the beam splitter. The strength of each circular component of this probe is proportional to the density of the carriers with each spin orientation. We use a quarter-wave plate to convert the two circular components to two linear polarizations that are orthogonal. We then use a Wollaston prism to separate them, and we measure them by a balanced detector and a lock-in amplifier. The voltage signal measured is proportional to the spin density, and it can be converted to the spin density by calibration.

With this system, we can detect S, N, and ΔN as a function of the probe delay with a time resolution of 100 fs and as a function of space by moving the probe laser spot with respect to the pump spots, with a spatial resolution of 1–2 μm. From the magnitudes of the S and ΔN profiles, we can determine the nanoscale transport length of spin and charge. The smallest detectable distance is solely determined by the SNR of the detection. In practice, we can detect a distance of 0.1 nm traveled by the carriers in GaAs samples.

C. Intrinsic Inverse Spin Hall Effect

In the spin Hall effect, a charge current produces a transverse pure spin current due to the spin-dependent scattering between electrons and impurities, as a result of the spin-orbit coupling. Recently, it has been extensively studied both theoretically [96–109] and experimentally [40,41,43,44,61,110,111]. Based on the same physics mechanism, a pure spin current can generate a transverse charge current. Such an inverse spin Hall effect has also been proposed [97] and experimentally observed [61,112,113]. In contrast to these extrinsic effects that are caused by scattering, the intrinsic spin Hall effect that does not rely on scattering has been proposed as well [99,100,114,115]. This effect can have important applications in nanoscale devices where the transport is dominated by ballistic carriers.

The combination of the QUIC and high-resolution pump–probe techniques allow us to time resolve the spin Hall dynamics in the ballistic regime [68]. In the experiments, we instantaneously inject a transient ballistic pure spin current in undoped GaAs multiple-quantum-well samples by the QUIC technique. After injection, the pure spin current decays due to scattering. By time resolving the decay, we can determine the scattering time. Then, by simultaneously monitoring the dynamics of the generated transverse charge current, we can determine whether the transverse current is generated before the first scattering event. This can provide unambiguous evidence for the intrinsic effect.

Figure 4 shows our observation of the intrinsic inverse spin Hall effect [68]. Several samples with similar structures were studied; here we show the measurement performed with a 40-period $GaAs/Al_{0.3}Ga_{0.7}As$ multiple-quantum-well sample with a well width of 7.4 nm. The sample is cooled to 10 K by a closed-cycle cryostat (Advanced Research Systems). A pure spin current is injected along the $\hat{x}$ direction by a pair of ultrafast pulses with wavelengths of 1500 and 750 nm that are perpendicularly linearly polarized. First, we acquire the profile of N by scanning a probe spot with wavelength 790 nm in the x–y plane with a fixed probe delay of 0.5 ps, as shown in Fig. 4(a). The Gaussian-shaped profile is consistent with the shape of the laser spots.

Because the two spin systems are injected with opposite average velocities along $\hat{x}$, the profiles of the two spin systems should separate along $\hat{x}$, resulting in a derivativelike S profile, as illustrated in Figs. 2(c) and 2(d). We measure S as we scan the probe spot along the $\hat{x}$ direction with $y = 1$ μm [white horizontal line in Fig. 4(a)]. The results are shown in Fig. 4(b). From the magnitude of this derivativelike profile, we deduce that at $\tau = 0.5$ ps, $\Delta x = 17$ nm. Because of the inverse spin Hall effect, we expect the profile of N to move along the transverse direction, $\hat{y}$. To monitor that transport, we measure ΔN as we scan the probe spot along $\hat{y}$ with $x = 1$ μm [white vertical line in Fig. 4(a)]. The derivativelike profile of ΔN, shown in Fig. 4(c), confirms that the charge transport occurs along $\hat{y}$. From this profile, we deduce $\Delta y = 0.3$ nm.

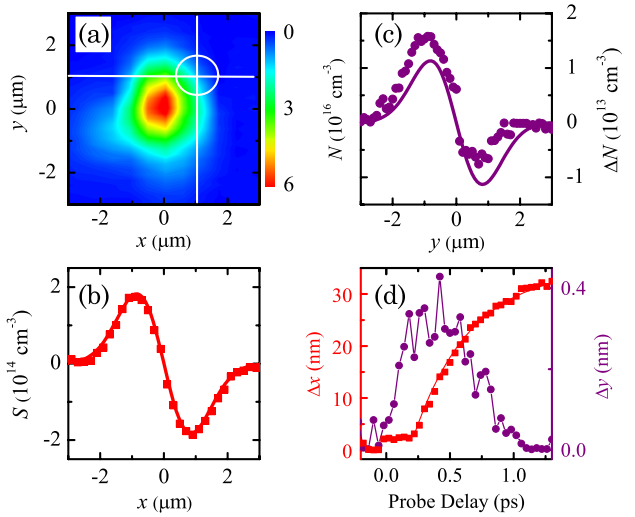

Fig. 4. (Color online) (a) Profile of N measured by scanning the probe spot in the x–y plane with a probe delay of 0.5 ps. The sample temperature is 10 K, and the peak carrier density is 6×10^{16} cm^{-3}. (b), (c) Spin density (S) and electron accumulation (ΔN) measured by scanning the probe spot along the horizontal line and the vertical line, respectively. (d) Deduced Δx (solid squares) and Δy (solid circles) as a function of the probe delay.

Next, we fix the probe spot at $x = y = 1$ μm [white circle in Fig. 4(a)] and simultaneously measure S and ΔN as we scan the probe delay. Figure 4(d) shows the Δx (solid squares, left axis) and Δy (solid circles, right axis) deduced from the measured S and ΔN as a function of the probe delay. To model the pure spin transport, we assume that the average velocity of each spin system decays exponentially, with a momentum relaxation time of τ_m. Hence, $\Delta x = \Delta x_0[1 - \exp(-\tau/\tau_m)]$, where Δx_0 is the final transport length. Using this equation, we fit the data (solid line) to deduce $\tau_m = 0.45$ ps. If the transverse charge current is induced via the extrinsic inverse spin Hall effect, it is expected to build up on a much longer time scale because it takes multiple electron-hole or electron-impurity scattering events to establish the transverse current. However, the simultaneously measured Δy reaches a peak before 0.45 ps. Because the transverse charge current density is proportional to the time-derivative of Δy, it peaks even earlier. Hence, the transverse current is generated before scattering. Because we can safely exclude the extrinsic inverse spin Hall effect in this scattering-free ballistic regime [99,100,114–116], we conclude that the observed inverse spin Hall effect is intrinsic. Our results are also consistent with a recent observation of the intrinsic spin Hall effect in HgTe nanostructures [117].

D. Time-Resolved Spin-Polarized Charge Currents

As shown in Fig. 1(c), a spin-polarized charge current is injected when the two pump pulses are both circularly polarized with the same sign. Previously, all-optical injections of spin-polarized charge currents have been demonstrated through the QUIC technique [95] and by the spin photogalvanic effect [118–126]. However, in these studies the currents were detected by steady-state electrical techniques that are not sensitive to spin. Hence, the currents were not time resolved and the spin polarization was not determined.

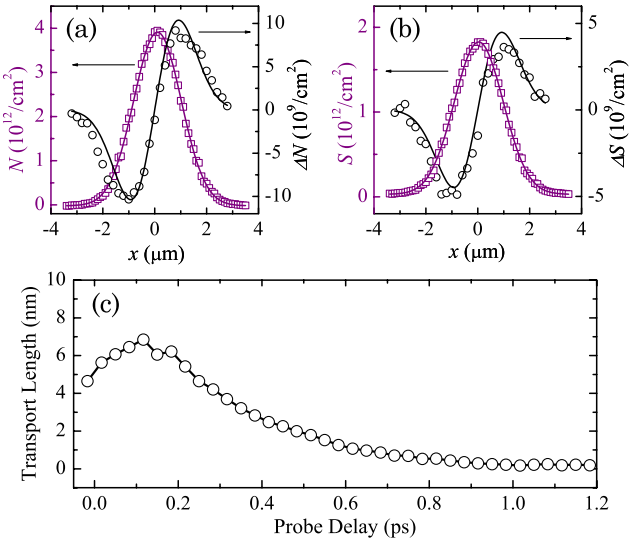

Fig. 5. (Color online) Spatially and temporally resolved ballistic spin-polarized charge current injected by the QUIC technique in a 400 nm bulk GaAs sample at room temperature. (a), (b) Spatial profiles of N [squares in (a)], ΔN [(circles in (a)], S [squares in (b)], and ΔS [circles in (b)] measured by scanning the probe spot along $\hat{x}$ with a fixed probe delay of 0.3 ps. (c) Position of the center of the electron density profile as a function of the probe delay.

The high-resolution pump–probe technique allows us to study the dynamics of the spin-polarized charge currents injected by the QUIC technique [63]. The experiment was performed on a 400 nm bulk GaAs sample at room temperature and a 10-period 14 nm GaAs multiple-quantum-well sample at 90 K. Similar results were obtained from both samples. Figure 5 summarizes the experimental results from the bulk sample. A pair of circularly polarized pulses with wavelengths of 1500 and 750 nm is used to inject the ballistic spin-polarized charge current. First, with a probe delay of 0.3 ps, we measure the spatial profiles of the carrier density [squares in Fig. 5(a)] and spin density [squares in Fig. 5(b)] by scanning the probe spot along $\hat{x}$ while modulating the pump intensity with a chopper. The Gaussian profiles are consistent with the shape and size of the laser spots. Next, we modulate the relative phase $\Delta\phi$ so that the $\hat{x}$ component of the injected current density is modulated. This allows us to detect ΔN (circles in A) and ΔS (circles in B) as we scan the probe spot along $\hat{x}$. Here, ΔS is defined in a similar way as ΔN, and it can be viewed as the accumulation of spin induced by the transport of spin-polarized carriers. By comparing the two profiles shown in Fig. 5(a), we deduced a carrier transport length of about 4 nm. By comparing the profiles of ΔN and ΔS, we found that the spin polarization of the current is about 50%.

These measurements were repeated with different probe delays in order to time resolve the transport. The results are shown in Fig. 5(c). Upon injection, the electrons move along $+\hat{x}$. Because the holes are injected with opposite momentum, according to crystal-momentum conservation, they move along $-\hat{x}$. Once the electrons and holes separate, a space charge field develops, slowing down and eventually stopping the motion of the electrons and holes. Then, the space charge field becomes a driving force to pull the electrons and holes back to a common location. Because throughout the entire process strong phonon and intercarrier scattering occurs, this oscillation is strongly damped. The dynamics exist only for less than 1 ps. From the measured ΔS, we found that the spin polarization of the current remains about 50% during this process.

E. Efficiency of the Quantum Interference to Inject Pure Spin Currents

We have also used the high-resolution technique to study the power dependence of pure spin current injection. For efficient current injection and precise control of pure spin currents with the QUIC technique, it is important to know how the injected spin current density varies with the intensities of the excitation laser pulses. It was known that the average velocity of each spin system in the injected pure spin current depends on the relative strength of the two transition pathways driven by the two laser pulses. This is similar to the classical interference of two light beams, where the contrast of the interference pattern is determined by the relative intensity of the two beams. In this case, the best contrast is achieved when the two beams are of the same intensity.

To investigate this issue, we studied the current injection efficiency as a function of the relative strength of the two transition pathways driven by the two laser pulses [64]. This is done by measuring the spin transport length as we vary the carrier density injected by each individual pulse, but we keep the total density unchanged. Under this condition, the spin

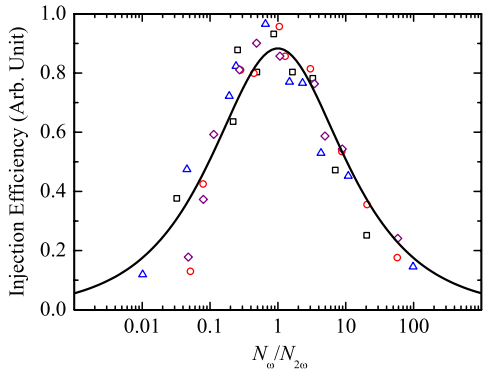

Fig. 6. (Color online) Current injection efficiency as a function of $N_\omega/N_{2\omega}$. In each set of measurements, the total electron density is kept constant when $n_\omega/n_{2\omega}$ is varied. The squares, circles, and triangles show data measured from a 400 nm bulk GaAs sample at room temperature, with the total carrier density of 1.4, 2.5, and 5.5×10^{17} cm^{-3}, respectively. The diamonds represent data measured from a multiple-quantum-well sample at 80 K, with total electron density of 1.0×10^{17} cm^{-3}.

transport length is only determined by the injected average velocity because the momentum relaxation has the same influence on all of the measurements. Figure 6 summarizes results from measurements performed on two samples under different conditions. We found that under our experimental conditions, the average velocity is determined by $N_\omega/N_{2\omega}$ in the same way as classical interference (solid line in Fig. 6), as predicted by a model based on Fermi's golden rule [57,127]. As a consequence, the density of the injected pure spin current increases monotonically with the excitation intensities [64].

4. DIRECT OPTICAL DETECTION OF BALLISTIC CURRENTS

In the previous section, the ballistic transport is studied by measuring the position of the carriers as a function of time. In order to overcome the limit on the spatial resolution imposed by diffraction, we used a derivative-detection scheme. However, it is desirable to have a technique that directly senses the velocity of carriers. In this section, we review our demonstrations of a second-order nonlinear optical effect induced by currents. Generally speaking, a flow of spin or charge current breaks the inversion symmetry of the material, allowing second-order responses. We will first discuss the experimental setup and procedures and then describe the demonstration of SHG induced by pure spin currents and pure charge currents.

A. Second-Harmonic Generation Induced by Pure Spin Currents

The SHG induced by pure spin currents was recently predicted by Wang *et al.* [128]. This effect is closely related to the well-known effect of Faraday rotation. The polarization direction of linearly polarized light rotates when propagating through a medium with a magnetic field applied along the propagation direction, with a rotation angle determined by the field strength and the length of the media. In a semiconductor, an electron with a certain spin orientation has an effective magnetic field, and it can also cause Faraday rotation of an incident light. In this process, the rotation angle is determined by the detuning between the frequency of the light and the interband transition frequency of the electron. In fact, this effect has been extensively used for optical detection of spin in semiconductors. However, in a pure spin current, every electron is accompanied by another electron with an opposite crystal momentum and an opposite spin orientation. Hence, the Faraday rotation caused by these two electrons seems to cancel, and there seems to be no optical effect. However, Wang and his co-workers [128] recognized that the electric field of the incident light would accelerate one electron but decelerate the other at any instant of time. This will change the detuning of the two electrons oppositely. Thus, the Faraday rotation caused by the two electrons is not exactly canceled, leaving a net second-order nonlinear optical susceptibility that is proportional to the current density [128].

Figure 7 illustrates the experimental setup we used to observe the SHG induced by a pure spin current [65]. It is similar to the high-resolution pump–probe system shown in Fig. 3. The pure spin current is still injected by the pair of $\omega/2\omega$ pulses that are obtained from the signal output of the OPO and its second-harmonic (SH), as discussed in Subsection 3.B. To observe the induced SHG, the idler output of the OPO with a central wavelength of 1760 nm, an intensity temporal width of 170 fs, and a pulse energy of 0.1 nJ, is used as the probe pulse. It is focused to a spot size of 2.1 μm from the back side of the sample. The probe pulse is linearly polarized along $\hat{x}$, which is the direction of the current flow. The expected SH of the probe pulse with a central wavelength of 880 nm is collected by the pump-focusing lens, and it is sent to a silicon photodiode. A combination of bandpass and color filters is used in front of the photodiode in order to block the unwanted beams, including the reflected and scattered pumps, the transmitted probe, and the photoluminescence of the sample.

We use a homodyne detection scheme to amplify the weak SH signal induced by the current by a vectorial addition with a local oscillator [129]. The local oscillator has the same frequency and ideally the same phase, but with a much larger amplitude. In our experiment, the surface SHG of the GaAs sample is used as the local oscillator for simplicity. The total SH intensity is a result of the interference of the two fields:

$$I = (c\epsilon_0/2)(\mathcal{E}_{LO} + \mathcal{E}_J)^2, \tag{3}$$

where c and ϵ_0 are the speed of light and the dielectric constant in a vacuum, respectively. We write this total SH intensity as

$$I = I_{LO} + \Delta I, \tag{4}$$

where

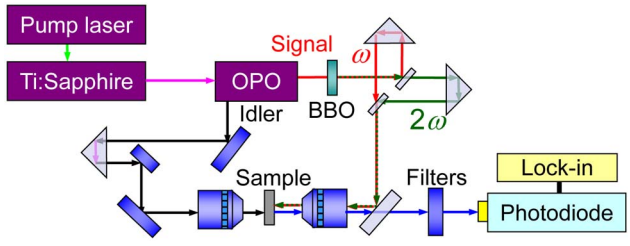

Fig. 7. (Color online) Experimental setup used to inject ballistic pure spin currents by the QUIC technique and observe the induced SHG.

$$I_{LO} = (c\epsilon_0/2)\mathcal{E}_{LO}^2 \tag{5}$$

is the intensity of the local oscillator, and

$$\Delta I = (c\epsilon_0/2)(2\mathcal{E}_{LO}\mathcal{E}_J + \mathcal{E}_J^2) \tag{6}$$

is the change of the total intensity due to the current-induced SHG. The silicon photodiode has a response time much longer than the pulse duration of the SH, and a size much larger than the focused beam. It integrates the intensity of the SH in both time and space, and it outputs a voltage signal that is proportional to the average power of the SH beam. The power corresponding to I_{LO}, P_{LO}, is measured by modulating the intensity of the probe pulse with an optical chopper, with the current-injecting pulses blocked. We find that $P_{LO} = 4$ nW. The optical power corresponding to ΔI, ΔP, is measured by modulating the injected current density, which is achieved by modulating $\Delta\phi$ with the electro-optic phase modulator [64]. We found that under our experimental conditions, the maximum value of ΔP is below 0.1 nW. Hence, $\mathcal{E}_{LO} \gg \mathcal{E}_J$. Because the second term in ΔI is then negligible, the optical power detected in this homodyne detection scheme, ΔP, is proportional to the amplitude of the optical field of the SH induced by the current and is therefore proportional to the current density at the probing location and the probing time.

Figure 8 shows an example of the detected SH signal as a function of the probe delay [65]. The sample is a 400 nm bulk GaAs crystal grown along the [100] direction, cooled to 10 K. In this measurement, the two pump pulses inject a total carrier density of $4 \times 10^{17}/\text{cm}^3$. With the average velocity of each spin system estimated to be about 30 nm/ps, the charge current density of each spin system is about 3×10^4 A/cm^2. A peak signal of ΔP of about 4 pW was observed. The signal decreases rapidly with the probe delay, showing the fast decay of the pure spin current due to momentum relaxation of each spin system, which is caused by scattering. However, the decay is clearly not pulse-width limited.

In the homodyne detection scheme, the total SH intensity is determined by the electric field amplitudes of both the surface SH and the current-induced SH. For our purpose, it is sufficient to write the former as

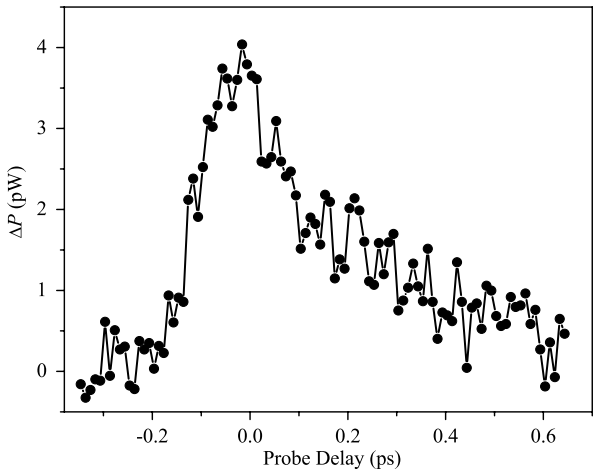

Fig. 8. SHG induced by the pure spin current.

$$\mathcal{E}_{LO} = A_{LO}\mathcal{E}_p^2, \tag{7}$$

where $\mathcal{E}_p$ is the field amplitude of the probe pulse (1760 nm) and A_{LO} is a parameter that can be determined experimentally: using Eq. (5),

$$A_{LO}^2 = (c\epsilon_0/2)\frac{I_{LO}}{I_p^2}, \tag{8}$$

with I_P the intensity of the probe. The field amplitude of the current-induced SH can be obtained by solving the coupled-wave equations [130]:

$$\mathcal{E}_J = A_J\mathcal{E}_p^2, \tag{9}$$

where

$$A_J = \frac{\pi L\chi_J^{(2)}}{n^2\lambda}, \tag{10}$$

where L and n are the thickness and the index of refraction of the sample, respectively, and λ is the wavelength of the SH in vacuum. Here, we have ignored the phase difference between $\mathcal{E}_{LO}$ and $\mathcal{E}_J$. This assumption is reasonable because the sample thickness is smaller than the coherence length and most currents are injected near the sample surface.

From Eqs. (5) and (6), we have

$$I_{LO} = (c\epsilon_0/2)A_{LO}^2\mathcal{E}_p^4 \tag{11}$$

and

$$\Delta I = (c\epsilon_0/2)(2A_{LO}A_J + A_J^2)\mathcal{E}_p^4 \approx (c\epsilon_0/2)(2A_{LO}A_J)\mathcal{E}_p^4, \tag{12}$$

because the intensity of the local oscillator is much higher than the current-induced SH. Hence

$$\frac{\Delta I}{I_{LO}} = \frac{2A_J}{A_{LO}}. \tag{13}$$

Collecting Eqs. (8), (10), and (13), we arrive at our final expression for the current-induced second-order susceptibility,

$$\chi_J^{(2)} = \frac{n^2\lambda}{2\pi L}\left(\frac{\Delta I}{I_{LO}}\right)\left(\frac{c\epsilon_0}{2}\right)^{1/2}\frac{I_{LO}^{1/2}}{I_p}. \tag{14}$$

Each intensity, ΔI, I_{LO}, and I_p, is a Gaussian function of time with a width on the order of 100 fs and has a Gaussian shape in space with a width of about 2 μm. The peak intensity can be calculated from the measured time-averaged power of the corresponding component, ΔP, P_{LO}, or P_p, using the relation

$$I \approx \frac{P}{f}\frac{1}{\tau}\frac{1}{\pi w^2}, \tag{15}$$

where f, τ, and w are the repetition rate of the laser (i.e., number of pulses per second), the temporal width of the pulse, and the width of the laser spot.

From the measurement, we have $P_p = 10$ mW, $P_{LO} = 4$ nW, and $\Delta P = 4$ pW. Using Eq. (15) with $f = 8 \times 10^7$ Hz, $\tau = 200$ fs, and $w = 2$ μm, the corresponding peak

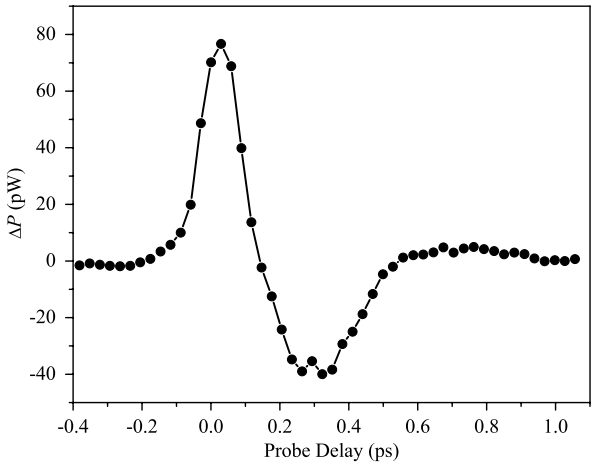

Fig. 9. SHG induced by the pure charge current.

intensities are $I_p = 10^{14}$ W/m^2, $I_{LO} = 4 \times 10^7$ W/m^2, and $\Delta I = 2 \times 10^5$ W/m^2, respectively. Using these values in Eq. (14), with $n = 3.6$, $\lambda = 880$ nm, $L = 400$ nm, $c = 3 \times 10^8$ m/s, and $\epsilon_0 = 8.85 \times 10^{-12}$ C^2/Nm^2, we find $\chi_J^{(2)} \approx 0.01$ pm/V, when the charge current density of each spin system is 3×10^4 A/cm^2 [65].

B. Second-Harmonic Generation Induced by Pure Charge Currents

Previously, it has been predicted that a charge current can also induce SHG [131]. We demonstrated this effect with a similar technique and procedure [132]. By using a pair of laser pulses that are both linearly polarized along $\hat{x}$, a ballistic pure charge current is injected along $\hat{x}$, as illustrated in Fig. 1(a). The same experimental setup as shown in Fig. 7 was used to observe the SHG induced by the injected charge current. Figure 9 shows an example of the experimental results of the same bulk GaAs sample cooled to 10 K. In this measurement, the injected current density is estimated to be 10^5 A/cm^2. A peak signal of about 80 pW was observed. We also found that the signal oscillates, due to the expected plasma oscillation: the electrons and holes are injected with opposite crystal momenta. Once they separate, a strongly nonuniform space charge field develops, which decelerates the carriers and causes the current density to drop. After the carriers reach their maximum displacements, with the current density dropping to zero, they are driven back toward the origin by the space charge field, giving rise to a negative current. As shown in Fig. 9, such a plasma oscillation is strongly damped, due to scattering and the field inhomogeneity [133]. By using the procedure described in Subsection 4.A., we deduce the induced second-order nonlinear susceptibility to be on the order of 0.05 pm/V for such a current density [132]. This is consistent with the theoretical value of 0.07 pm/V [131].

It is well known that an electric field can induce SHG [134–139]. Although the injected current in our experiment is accompanied by a space charge field, we can safely rule out the latter as the cause of SHG: the space charge field is proportional to the charge separation, and hence it is delayed with respect to the current density, J, by approximately a quarter period. Such a lag has been confirmed in our previous high-resolution pump–probe experiments, where the charge separation was found to reach a peak after more than 100 fs [62,63]. Here, we observed the peak SHG around zero probe delay. Hence, the all-optical time-resolved technique has the advantage to unambiguously distinguish the field-induced and the current-induced SHG effects. This can be quite difficult in steady-state measurements where the current is proportional to the field [140].

5. SUMMARY

We have discussed our recent studies on ballistic charge and spin currents using nonlinear optical techniques. By using quantum interference between one-photon and two-photon absorption pathways, one can inject different types of ballistic currents, including pure charge current, pure spin current, and spin-polarized charge currents, by simply choosing different polarization configurations of the pump laser pulses. A high-resolution pump–probe technique is used to spatially and temporally resolve these ballistic currents. By using a derivative-detection scheme, we can detect motion of carriers as short as 0.1 nm. We have observed the intrinsic inverse spin Hall effect in the ballistic regime, time-resolved ballistic spin-polarized charge currents, and we studied the efficiency of current injection by quantum interference. Following theoretical predictions, we have demonstrated that charge and spin currents can induce second-order nonlinear optical effects, with the nonlinear susceptibility being proportional to the current density. These nonlinear optical effects can be used for nondestructive, noninvasive, and real-time imaging of currents.

ACKNOWLEDGMENTS

The research results reviewed in this article were obtained in collaboration with Lalani Werake, Karl Higley, Jacob Khurgin, and Eugune Ya Sherman. We acknowledge very helpful discussions with Ren-Bao Liu, Bang-Fen Zhu, and Jing Wang on the physical interpretation of the SHG induced by pure spin currents. We thank John Prineas for providing high-quality GaAs samples. We acknowledge support from the National Science Foundation (DMR-0954486).

REFERENCES

1. D. A. Neamen, *Semiconductor Physics and Devices* (McGraw-Hill, 2002).
2. J. Shah, *Ultrafast Spectroscopy of Semiconductors and Semiconductor Nanostructures* (Springer, 1996).
3. J. Hegarty, L. Goldner, and M. D. Sturge, "Localized and delocalized two-dimensional excitons in GaAs-AlGaAs multiple-quantum-well structures," Phys. Rev. B **30**, 7346–7348 (1984).
4. K. Hattori, T. Mori, H. Okamoto, and Y. Hamakawa, "Carrier transport property in the amorphous silicon/amorphous silicon carbide multilayer studied by the transient grating technique," Appl. Phys. Lett. **51**, 1259–1261 (1987).
5. H. Schwab, K.-H. Pantke, J. M. Hvam, and C. Klingshirn, "Measurements of exciton diffusion by degenerate four-wave mixing in CdSSe," Phys. Rev. B **46**, 7528–7532 (1992).
6. J. Erland, B. S. Razbirin, K.-H. Pantke, V. G. Lyssenko, and J. M. Hvam, "Exciton diffusion in CdSe," Phys. Rev. B **47**, 3582–3587 (1993).
7. V. Mizeikis, V. G. Lyssenko, J. Erland, and J. M. Hvam, "Excitonic optical nonlinearities and transport in the layered compound semiconductor GaSe," Phys. Rev. B **51**, 16651–16659 (1995).

8. A. C. Schaefer, J. Erland, and D. G. Steel, "Nondiffusive excitonic transport in GaAs and the effects of momentum scattering," Phys. Rev. B **54**, R11046–R11049 (1996).
9. F. A. Majumder, H.-E. Swoboda, K. Kempf, and C. Klingshirn, "Electron-hole plasma expansion in the direct-band-gap semiconductors CdS and CdSe," Phys. Rev. B **32**, 2407–2418 (1985).
10. L. M. Smith, D. R. Wake, J. P. Wolfe, D. Levi, M. V. Klein, J. Klem, T. Henderson, and H. Morkoç, "Picosecond imaging of photoexcited carriers in quantum wells: anomalous lateral confinement at high densities," Phys. Rev. B **38**, 5788–5791 (1988).
11. L. M. Smith, J. S. Preston, J. P. Wolfe, D. R. Wake, J. Klem, T. Henderson, and H. Morkoç, "Phonon-wind-driven transport of photoexcited carriers in a semiconductor quantum well," Phys. Rev. B **39**, 1862–1870 (1989).
12. H. W. Yoon, D. R. Wake, J. P. Wolfe, and H. Morkoç, "In-plane transport of photoexcited carriers in GaAs quantum wells," Phys. Rev. B **46**, 13461–13470 (1992).
13. M. Achermann, B. A. Nechay, F. Morier-Genoud, A. Schertel, U. Siegner, and U. Keller, "Direct experimental observation of different diffusive transport regimes in semiconductor nanostructures," Phys. Rev. B **60**, 2101–2105 (1999).
14. B. A. Nechay, U. Siegner, F. Morier-Genoud, A. Schertel, and U. Keller, "Femtosecond near-field optical spectroscopy of implantation patterned semiconductors," Appl. Phys. Lett. **74**, 61–64 (1999).
15. H. Zhao, "Temperature dependence of ambipolar diffusion in silicon on insulator," Appl. Phys. Lett. **92**, 112104 (2008).
16. H. Zhao, M. Mower, and G. Vignale, "Ambipolar spin diffusion and D'yakonov-Perel' spin relaxation in GaAs quantum wells," Phys. Rev. B **79**, 115321 (2009).
17. B. A. Ruzicka, L. K. Werake, H. Zhao, S. Wang, and K. P. Loh, "Femtosecond pump-probe studies of reduced graphene oxide thin films," Appl. Phys. Lett. **96**, 173106 (2010).
18. B. A. Ruzicka, S. Wang, L. K. Werake, B. Weintrub, K. P. Loh, and H. Zhao, "Hot carrier diffusion in graphene," Phys. Rev. B **82**, 195414 (2010).
19. B. A. Ruzicka, L. K. Werake, H. Samassekou, and H. Zhao, "Ambipolar diffusion of photoexcited carriers in bulk GaAs," Appl. Phys. Lett. **97**, 262119 (2010).
20. N. Kumar, B. A. Ruzicka, N. P. Butch, P. Syers, K. Kirshenbaum, J. Paglione, and H. Zhao, "Spatially resolved femtosecond pump-probe study of topological insulator Bi_2Se_3," Phys. Rev. B **83**, 235306 (2011).
21. L.-L. Chao, G. S. Gargill III, E. Snoeks, T. Marshall, J. Petruzzello, and M. Pashley, "Diffusion lengths of excited carriers in CdZnSe quantum wells," Appl. Phys. Lett. **74**, 741–743 (1999).
22. F. P. Logue, D. T. Fewer, S. J. Hewlett, J. F. Heffernan, C. Jordan, P. Rees, J. F. Donegan, E. M. McCabe, J. Hegarty, S. Taniguchi, T. Hino, K. Nakano, and A. Ishibashi, "Optical measurement of the ambipolar diffusion length in a ZnCdSe-ZnSe single quantum well," J. Appl. Phys. **81**, 536–538 (1997).
23. A. Vertikov, I. Ozden, and A. Nurmikko, "Investigation of excess carrier diffusion in nitride semiconductors with near-field optical microscopy," Appl. Phys. Lett. **74**, 850–852 (1999).
24. V. Malyarchuk, J. W. Tomm, V. Talalaev, C. Lienau, F. Rinner, and M. Baeumler, "Nanoscopic measurements of surface recombination velocity and diffusion length in a semiconductor quantum well," Appl. Phys. Lett. **81**, 346–348 (2002).
25. H. Hillmer, A. Forchel, and C. W. Tu, "Enhancement of electron-hole pair mobilities in thin GaAs/AlGaAs quantum wells," Phys. Rev. B **45**, 1240–1245 (1992).
26. H. Akiyama, T. Matsusue, and H. Sakaki, "Carrier scattering and excitonic effects on electron-hole-pair diffusion in nondoped and *p*-type-modulation-doped $GaAs/Al_xGa_{1-x}As$ quantum-well structures," Phys. Rev. B **49**, 14523–14530 (1994).
27. S. A. Wolf, D. D. Awschalom, R. A. Buhrman, J. M. Daughton, S. von Molnar, M. L. Roukes, A. Y. Chtchelkanova, and D. M. Treger, "Spintronics: a spin-based electronics vision for the future," Science **294**, 1488–1495 (2001).
28. I. Žutić, J. Fabian, and S. Das Sarma, "Spintronics: fundamentals and applications," Rev. Mod. Phys. **76**, 323–410 (2004).
29. S. Datta and B. Das, "Electronic analog of the electro-optic modulator," Appl. Phys. Lett. **56**, 665–667 (1990).
30. D. Hägele, M. Oestreich, W. W. Rühle, N. Nestle, and K. Eberl, "Spin transport in GaAs," Appl. Phys. Lett. **73**, 1580–1582 (1998).
31. H. Sanada, I. Arata, Y. Ohno, Z. Chen, K. Kayanuma, Y. Oka, F. Matsukura, and H. Ohno, "Relaxation of photoinjected spins during drift transport in GaAs," Appl. Phys. Lett. **81**, 2788–2790 (2002).
32. T. Sogawa, H. Ando, and S. Ando, "Spin-transport dynamics of optically spin-polarized electrons in GaAs quantum wires," Phys. Rev. B **61**, 5535–5539 (2000).
33. T. Sogawa, P. V. Santos, S. K. Zhang, S. Eshlaghi, A. D. Wieck, and K. H. Ploog, "Transport and lifetime enhancement of photoexcited spins in GaAs by surface acoustic waves," Phys. Rev. Lett. **87**, 276601 (2001).
34. J. A. H. Stotz, R. Hey, P. V. Santos, and K. H. Ploog, "Coherent spin transport through dynamic quantum dots," Nat. Mater. **4**, 585–588 (2005).
35. O. D. D. Couto, F. Iikawa, J. Rudolph, R. Hey, and P. V. Santos, "Anisotropic spin transport in (110) GaAs quantum wells," Phys. Rev. Lett. **98**, 036603 (2007).
36. J. M. Kikkawa and D. D. Awschalom, "Lateral drag of spin coherence in gallium arsenide," Nature **397**, 139–141 (1999).
37. I. Malajovich, J. J. Berry, N. Samarth, and D. D. Awschalom, "Persistent sourcing of coherent spins for multifunctional semiconductor spintronics," Nature **411**, 770–772 (2001).
38. I. Malajovich, J. M. Kikkawa, D. D. Awschalom, J. J. Berry, and N. Samarth, "Coherent transfer of spin through a semiconductor heterointerface," Phys. Rev. Lett. **84**, 1015–1018 (2000).
39. S. A. Crooker and D. L. Smith, "Imaging spin flows in semiconductors subject to electric, magnetic, and strain fields," Phys. Rev. Lett. **94**, 236601 (2005).
40. Y. K. Kato, R. C. Myers, A. C. Gossard, and D. D. Awschalom, "Observation of the spin Hall effect in semiconductors," Science **306**, 1910–1913 (2004).
41. V. Sih, R. C. Myers, Y. K. Kato, W. H. Lau, A. C. Gossard, and D. D. Awschalom, "Spatial imaging of the spin Hall effect and current-induced polarization in two-dimensional electron gases," Nat. Phys. **1**, 31–35 (2005).
42. V. Sih, W. H. Lau, R. C. Myers, V. R. Horowitz, A. C. Gossard, and D. D. Awschalom, "Generating spin currents in semiconductors with the spin Hall effect," Phys. Rev. Lett. **97**, 096605 (2006).
43. N. P. Stern, S. Ghosh, G. Xiang, M. Zhu, N. Samarth, and D. D. Awschalom, "Current-induced polarization and the spin Hall effect at room temperature," Phys. Rev. Lett. **97**, 126603 (2006).
44. N. P. Stern, D. W. Steuerman, S. Mack, A. C. Gossard, and D. D. Awschalom, "Time-resolved dynamics of the spin Hall effect," Nat. Phys. **4**, 843–846 (2008).
45. S. A. Crooker, M. Furis, X. Lou, C. Adelmann, D. L. Smith, C. J. Palmstrom, and P. A. Crowell, "Imaging spin transport in lateral ferromagnet/semiconductor structures," Science **309**, 2191–2195 (2005).
46. C. P. Weber, N. Gedik, J. E. Moore, J. Orenstein, J. Stephens, and D. D. Awschalom, "Observation of spin Coulomb drag in a two-dimensional electron gas," Nature **437**, 1330–1333 (2005).
47. S. G. Carter, Z. Chen, and S. T. Cundiff, "Optical measurement and control of spin diffusion in *n*-doped GaAs quantum wells," Phys. Rev. Lett. **97**, 136602 (2006).
48. C. P. Weber, J. Orenstein, B. A. Bernevig, S. C. Zhang, J. Stephens, and D. D. Awschalom, "Nondiffusive spin dynamics in a two-dimensional electron gas," Phys. Rev. Lett. **98**, 076604 (2007).
49. J. D. Koralek, C. P. Weber, J. Orenstein, B. A. Bernevig, S. C. Zhang, S. Mack, and D. D. Awschalom, "Emergence of the persistent spin helix in semiconductor quantum wells," Nature **458**, 610–613 (2009).
50. E. Dupont, P. B. Corkum, H. C. Liu, M. Buchanan, and Z. R. Wasilewski, "Phase-controlled currents in semiconductors," Phys. Rev. Lett. **74**, 3596–3599 (1995).
51. R. Atanasov, A. Haché, J. L. P. Hughes, H. M. van Driel, and J. E. Sipe, "Coherent control of photocurrent generation in bulk semiconductors," Phys. Rev. Lett. **76**, 1703–1706 (1996).
52. A. Haché, Y. Kostoulas, R. Atanasov, J. L. P. Hughes, J. E. Sipe, and H. M. van Driel, "Observation of coherently controlled

photocurrent in unbiased, bulk GaAs," Phys. Rev. Lett. **78**, 306–309 (1997).
53. T. M. Fortier, P. A. Roos, D. J. Jones, S. T. Cundiff, R. D. R. Bhat, and J. E. Sipe, "Carrier-envelope phase-controlled quantum interference of injected photocurrents in semiconductors," Phys. Rev. Lett. **92**, 147403 (2004).
54. P. A. Roos, X. Li, R. P. Smith, J. A. Pipis, T. M. Fortier, and S. T. Cundiff, "Solid-state carrier-envelope phase stabilization via quantum interference control of injected photocurrents," Opt. Lett. **30**, 735–737 (2005).
55. D. Cote, J. M. Fraser, M. DeCamp, P. H. Bucksbaum, and H. M. van Driel, "THz emission from coherently controlled photocurrents in GaAs," Appl. Phys. Lett. **75**, 3959–3961 (1999).
56. M. J. Stevens, A. Najmaie, R. D. R. Bhat, J. E. Sipe, H. M. van Driel, and A. L. Smirl, "Optical injection and coherent control of a ballistic charge current in GaAs/AlGaAs quantum wells," J. Appl. Phys. **94**, 4999–5004 (2003).
57. R. D. R. Bhat and J. E. Sipe, "Optically injected spin currents in semiconductors," Phys. Rev. Lett. **85**, 5432–5435 (2000).
58. M. J. Stevens, A. L. Smirl, R. D. R. Bhat, A. Najmaie, J. E. Sipe, and H. M. van Driel, "Quantum interference control of ballistic pure spin currents in semiconductors," Phys. Rev. Lett. **90**, 136603 (2003).
59. J. Hübner, W. W. Rühle, M. Klude, D. Hommel, R. D. R. Bhat, J. E. Sipe, and H. M. van Driel, "Direct observation of optically injected spin-polarized currents in semiconductors," Phys. Rev. Lett. **90**, 216601 (2003).
60. H. Zhao, A. L. Smirl, and H. M. van Driel, "Temporally and spatially resolved ballistic pure spin transport," Phys. Rev. B **75**, 075305 (2007).
61. H. Zhao, E. J. Loren, H. M. van Driel, and A. L. Smirl, "Coherence control of Hall charge and spin currents," Phys. Rev. Lett. **96**, 246601 (2006).
62. H. Zhao, E. J. Loren, A. L. Smirl, and H. M. van Driel, "Dynamics of charge currents ballistically injected in GaAs by quantum interference," J. Appl. Phys. **103**, 053510 (2008).
63. B. A. Ruzicka, K. Higley, L. K. Werake, and H. Zhao, "All-optical generation and detection of subpicosecond ac spin-current pulses in GaAs," Phys. Rev. B **78**, 045314 (2008).
64. B. A. Ruzicka and H. Zhao, "Power dependence of pure spin current injection by quantum interference," Phys. Rev. B **79**, 155204 (2009).
65. L. K. Werake and H. Zhao, "Observation of second-harmonic generation induced by pure spin currents," Nat. Phys. **6**, 875–878 (2010).
66. E. Loren, H. Zhao, and A. L. Smirl, "All-optical injection and detection of ballistic charge currents in germanium," J. Appl. Phys. **108**, 083111 (2010).
67. H. Zhao and A. L. Smirl, "Injection and detection of ballistic electrical currents in silicon," Appl. Phys. Lett. **97**, 212106 (2010).
68. L. K. Werake, B. A. Ruzicka, and H. Zhao, "Observation of intrinsic inverse spin Hall effect," Phys. Rev. Lett. **106**, 107205 (2011).
69. C. Sames, J. M. Menard, M. Betz, A. L. Smirl, and H. M. van Driel, "All-optical coherently controlled terahertz ac charge currents from excitons in semiconductors," Phys. Rev. B **79**, 045208 (2009).
70. M. Spasenović, M. Betz, L. Costa, and H. M. van Driel, "All-optical coherent control of electrical currents in centrosymmetric semiconductors," Phys. Rev. B **77**, 085201 (2008).
71. L. Costa, M. Betz, M. Spasenovic, A. D. Bristow, and H. M. van Driel, "All-optical injection of ballistic electrical currents in unbiased silicon," Nat. Phys. **3**, 632–635 (2007).
72. R. W. Newson, A. A. Green, M. C. Hersam, and H. M. van Driel, "Coherent injection and control of ballistic charge currents in single-walled carbon nanotubes and graphite," Phys. Rev. B **83**, 115421 (2011).
73. C. Aversa and J. E. Sipe, "Coherent current control in semiconductors: a susceptibility perspective," IEEE J. Quantum Electron. **32**, 1570–1573 (1996).
74. D. Cote and H. M. van Driel, "Quantum interference control of electrical currents in GaAs," IEEE J. Quantum Electron. **34**, 1144–1154 (1998).
75. P. Roos, Q. Quraishi, S. Cundiff, R. Bhat, and J. Sipe, "Characterization of quantum interference control of injected currents in LT-GaAs for carrier-envelope phase measurements," Opt. Express **11**, 2081–2090 (2003).
76. P. A. Roos, X. Li, J. A. Pipis, T. M. Fortier, S. T. Cundiff, R. D. R. Bhat, and J. E. Sipe, "Characterization of carrier-envelope phase-sensitive photocurrent injection in a semiconductor," J. Opt. Soc. Am. B **22**, 362–368 (2005).
77. R. W. Newson, J. M. Menard, C. Sames, M. Betz, and H. M. van Driel, "Coherently controlled ballistic charge currents injected in single-walled carbon nanotubes and graphite," Nano Lett. **8**, 1586–1589 (2008).
78. D. Sun, C. Divin, J. Rioux, J. E. Sipe, C. Berger, W. A. de Heer, P. N. First, and T. B. Norris, "Coherent control of ballistic photocurrents in multilayer epitaxial graphene using quantum interference," Nano Lett. **10**, 1293–1296 (2010).
79. E. Alphandery, R. J. Nicholas, N. J. Mason, B. Zhang, P. Möck, and G. R. Booker, "Self-assembled InSb quantum dots grown on GaSb: a photoluminescence, magnetoluminescence, and atomic force microscopy study," Appl. Phys. Lett. **74**, 2041–2043 (1999).
80. Y. Kerachian, P. A. Marsden, and H. M. van Driel, "Dynamics of charge current gratings generated in GaAs by ultrafast quantum interference control," Phys. Rev. B **75**, 125205 (2007).
81. Y. Kerachian, H. M. van Driel, and A. L. Smirl, "Superposition of electron-hole density gratings in GaAs generated by quantum control of charge densities and charge currents," Phys. Rev. B **75**, 125206 (2007).
82. D. H. Marti, M. A. Dupertuis, and B. Deveaud, "Dynamics of optical injection of charge and spin currents in quantum wells," Phys. Rev. B **69**, 035335 (2004).
83. K. A. Pronin and A. D. Bandrauk, "Coherent control of electric currents in superlattices and molecular wires: effect of relaxation," Phys. Rev. B **69**, 195308 (2004).
84. H. T. Duc, T. Meier, and S. W. Koch, "Microscopic analysis of the coherent optical generation and the decay of charge and spin currents in semiconductor heterostructures," Phys. Rev. Lett. **95**, 086606 (2005).
85. D. H. Marti, M. A. Dupertuis, and B. Deveaud, "Optical injection of charge current in quantum wires: oscillations induced by excitonic effects," Phys. Rev. B **72**, 075357 (2005).
86. Y. Kerachian, P. Nemec, H. M. van Driel, and A. L. Smirl, "Pure spin current gratings in semiconductors generated by quantum interference," J. Appl. Phys. **96**, 430–434 (2004).
87. E. J. Loren, B. A. Ruzicka, L. K. Werake, H. Zhao, H. M. van Driel, and A. L. Smirl, "Optical injection and detection of ballistic pure spin currents in Ge," Appl. Phys. Lett. **95**, 092107 (2009).
88. F. J. Jedema, A. T. Filip, and B. J. van Wees, "Electrical spin injection and accumulation at room temperature in an all-metal mesoscopic spin valve," Nature **410**, 345–348 (2001).
89. S. K. Watson, R. M. Potok, C. M. Marcus, and V. Umansky, "Experimental realization of a quantum spin pump," Phys. Rev. Lett. **91**, 258301 (2003).
90. S. D. Ganichev, V. V. Bel'kov, S. A. Tarasenko, S. N. Danilov, S. Giglberger, C. Hoffmann, E. L. Ivchenko, D. Weiss, W. Wegscheider, C. Gerl, D. Schuh, J. Stahl, J. D. Boeck, G. Borghs, and W. Prettl, "Zero-bias spin separation," Nat. Phys. **2**, 609–613 (2006).
91. T. Seki, Y. Hasegawa, S. Mitani, S. Takahashi, H. Imamura, S. Maekawa, J. Nitta, and K. Takanashi, "Giant spin Hall effect in perpendicularly spin-polarized FePt/Au devices," Nat. Mater. **7**, 125–129 (2008).
92. K. Uchida, S. Takahashi, K. Harii, J. Ieda, W. Koshibae, K. Ando, S. Maekawa, and E. Saitoh, "Observation of the spin Seebeck effect," Nature **455**, 778–781 (2008).
93. T. Yang, T. Kimura, and Y. Otani, "Giant spin-accumulation signal and pure spin-current-induced reversible magnetization switching," Nat. Phys. **4**, 851–854 (2008).
94. S. M. Frolov, A. Venkatesan, W. Yu, J. A. Folk, and W. Wegscheider, "Electrical generation of pure spin currents in a two-dimensional electron gas," Phys. Rev. Lett. **102**, 116802 (2009).
95. M. J. Stevens, A. L. Smirl, R. D. R. Bhat, J. E. Sipe, and H. M. van Driel, "Coherent control of an optically injected ballistic spin-polarized current in bulk GaAs," J. Appl. Phys. **91**, 4382–4386 (2002).
96. M. I. D'yakonov and V. I. Perel, "Possibility of orienting electron spins with current," JETP Lett. **13**, 467–469 (1971).

97. J. E. Hirsch, "Spin Hall effect," Phys. Rev. Lett. **83**, 1834–1837 (1999).
98. S. F. Zhang, "Spin Hall effect in the presence of spin diffusion," Phys. Rev. Lett. **85**, 393–396 (2000).
99. S. Murakami, N. Nagaosa, and S. C. Zhang, "Dissipationless quantum spin current at room temperature," Science **301**, 1348–1351 (2003).
100. J. Sinova, D. Culcer, Q. Niu, N. A. Sinitsyn, T. Jungwirth, and A. H. MacDonald, "Universal intrinsic spin Hall effect," Phys. Rev. Lett. **92**, 126603 (2004).
101. E. G. Mishchenko, A. V. Shytov, and B. I. Halperin, "Spin current and polarization in impure two-dimensional electron systems with spin-orbit coupling," Phys. Rev. Lett. **93**, 226602 (2004).
102. L. Sheng, D. N. Sheng, and C. S. Ting, "Spin-Hall effect in two-dimensional electron systems with Rashba spin-orbit coupling and disorder," Phys. Rev. Lett. **94**, 016602 (2005).
103. C. L. Kane and E. J. Mele, "Quantum spin Hall effect in graphene," Phys. Rev. Lett. **95**, 226801 (2005).
104. S. Q. Shen, M. Ma, X. C. Xie, and F. C. Zhang, "Resonant spin Hall conductance in two-dimensional electron systems with a Rashba interaction in a perpendicular magnetic field," Phys. Rev. Lett. **92**, 256603 (2004).
105. S. Zhang and Z. Yang, "Intrinsic spin and orbital angular momentum Hall effect," Phys. Rev. Lett. **94**, 066602 (2005).
106. B. K. Nikolic, S. Souma, L. P. Zarbo, and J. Sinova, "Nonequilibrium spin Hall accumulation in ballistic semiconductor nanostructures," Phys. Rev. Lett. **95**, 046601 (2005).
107. B. A. Bernevig and S. C. Zhang, "Intrinsic spin Hall effect in the two-dimensional hole gas," Phys. Rev. Lett. **95**, 016801 (2005).
108. H. Engel, B. I. Halperin, and E. I. Rashba, "Theory of spin Hall conductivity in *n*-doped GaAs," Phys. Rev. Lett. **95**, 166605 (2005).
109. S. Murakami, N. Nagaosa, and S. C. Zhang, "Spin-Hall insulator," Phys. Rev. Lett. **93**, 156804 (2004).
110. J. Wunderlich, B. Kaestner, J. Sinova, and T. Jungwirth, "Experimental observation of the spin-Hall effect in a two-dimensional spin-orbit coupled semiconductor system," Phys. Rev. Lett. **94**, 047204 (2005).
111. E. S. Garlid, Q. O. Hu, M. K. Chan, C. J. Palmstrøm, and P. A. Crowell, "Electrical measurement of the direct spin Hall effect in $Fe/In_xGa_{1-x}As$ heterostructures," Phys. Rev. Lett. **105**, 156602 (2010).
112. S. O. Valenzuela and M. Tinkham, "Direct electronic measurement of the spin Hall effect," Nature **442**, 176–179 (2006).
113. T. Kimura, Y. Otani, T. Sato, S. Takahashi, and S. Maekawa, "Room-temperature reversible spin Hall effect," Phys. Rev. Lett. **98**, 156601 (2007).
114. J. Schliemann and D. Loss, "Dissipation effects in spin-Hall transport of electrons and holes," Phys. Rev. B **69**, 165315 (2004).
115. J. Inoue, G. E. W. Bauer, and L. W. Molenkamp, "Suppression of the persistent spin Hall current by defect scattering," Phys. Rev. B **70**, 041303 (2004).
116. E. Y. Sherman, A. Najmaie, H. M. van Driel, A. L. Smirl, and J. E. Sipe, "Ultrafast extrinsic spin-Hall currents," Solid State Commun. **139**, 439–446 (2006).
117. C. Brüne, A. Roth, E. G. Novik, M. König, H. Buhmann, E. M. Hankiewicz, W. Hanke, J. Sinova, and L. W. Molenkamp, "Evidence for the ballistic intrinsic spin Hall effect in HgTe nanostructures," Nat. Phys. **6**, 448–454 (2010).
118. S. D. Ganichev, H. Ketterl, W. Prettl, E. L. Ivchenko, and L. E. Vorobjev, "Circular photogalvanic effect induced by monopolar spin orientation in *p*-GaAs/AlGaAs multiple-quantum wells," Appl. Phys. Lett. **77**, 3146–3148 (2000).
119. S. D. Ganichev, V. V. Bel'kov, P. Schneider, E. L. Ivchenko, S. A. Tarasenko, W. Wegscheider, D. Weiss, D. Schuh, E. V. Beregulin, and W. Prettl, "Resonant inversion of the circular photogalvanic effect in *n*-doped quantum wells," Phys. Rev. B **68**, 035319 (2003).
120. H. Diehl, V. A. Shalygin, V. V. Bel'kov, C. Hoffmann, S. N. Danilov, T. Herrle, S. A. Tarasenko, D. Schuh, C. Gerl, W. Wegscheider, W. Prettl, and S. D. Ganichev, "Spin photocurrents in (110)-grown quantum well structures," New J. Phys. **9**, 349 (2007).
121. S. D. Ganichev, E. L. Ivchenko, S. N. Danilov, J. Eroms, W. Wegscheider, D. Weiss, and W. Prettl, "Conversion of spin into directed electric current in quantum wells," Phys. Rev. Lett. **86**, 4358–4361 (2001).
122. C. M. Wei, K. S. Cho, Y. F. Chen, Y. H. Peng, C. W. Chiu, and C. H. Kuan, "Photogalvanic effects for interband transition in *p*-$Si_{0.5}Ge_{0.5}$/Si multiple quantum wells," Appl. Phys. Lett. **91**, 252102 (2007).
123. K. S. Cho, C. T. Liang, Y. F. Chen, Y. Q. Tang, and B. Shen, "Spin-dependent photocurrent induced by Rashba-type spin splitting in $Al_{0.25}Ga_{0.75}N$/GaN heterostructures," Phys. Rev. B **75**, 085327 (2007).
124. K. S. Cho, Y. F. Chen, Y. Q. Tang, and B. Shen, "Photogalvanic effects for interband absorption in AlGaN/GaN superlattices," Appl. Phys. Lett. **90**, 041909 (2007).
125. X. W. He, B. Shen, Y. Q. Tang, N. Tang, C. M. Yin, F. J. Xu, Z. J. Yang, G. Y. Zhang, Y. H. Chen, C. G. Tang, and Z. G. Wang, "Circular photogalvanic effect of the two-dimensional electron gas in $Al_xGa_{1-x}N$/GaN heterostructures under uniaxial strain," Appl. Phys. Lett. **91**, 071912 (2007).
126. Y. Q. Tang, B. Shen, X. W. He, K. Han, N. Tang, W. H. Chen, Z. J. Yang, G. Y. Zhang, Y. H. Chen, C. G. Tang, Z. G. Wang, K. S. Cho, and Y. F. Chen, "Room-temperature spin-oriented photocurrent under near-infrared irradiation and comparison of optical means with Shubnikov de-Haas measurements in $Al_xGa_{1-x}N$/GaN heterostructures," Appl. Phys. Lett. **91**, 071920 (2007).
127. A. Najmaie, R. D. R. Bhat, and J. E. Sipe, "All-optical injection and control of spin and electrical currents in quantum wells," Phys. Rev. B **68**, 165348 (2003).
128. J. Wang, B. F. Zhu, and R. B. Liu, "Second-order nonlinear optical effects of spin currents," Phys. Rev. Lett. **104**, 256601 (2010).
129. P. C. D. Hobbs, *Building Electro-Optical Systems*, 2nd ed. (Wiley, 2009).
130. R. W. Boyd, *Nonlinear Optics*, 3rd ed. (Academic, 2008).
131. J. B. Khurgin, "Current induced second harmonic generation in semiconductors," Appl. Phys. Lett. **67**, 1113–1115 (1995).
132. B. A. Ruzicka, L. K. Werake, G. W. Xu, J. B. Khurgin, E. Y. Sherman, J. Z. Wu, and H. Zhao, "Second-harmonic generation induced by electric currents in GaAs," Phys. Rev. Lett. (to be published).
133. E. Y. Sherman, R. M. Abrarov, and J. E. Sipe, "Mode coupling and evolution in broken-symmetry plasmas," Phys. Rev. B **80**, 161308 (2009).
134. C. H. Lee, R. K. Chang, and N. Bloembergen, "Nonlinear electroreflectance in silicon and silver," Phys. Rev. Lett. **18**, 167–170 (1967).
135. K. Hakuta, L. Marmet, and B. P. Stoicheff, "Electric-field-induced second-harmonic generation with reduced absorption in atomic hydrogen," Phys. Rev. Lett. **66**, 596–599 (1991).
136. J. Bloch, J. G. Mihaychuk, and H. M. van Driel, "Electron photoinjection from silicon to ultrathin SiO_2 films via ambient oxygen," Phys. Rev. Lett. **77**, 920–923 (1996).
137. C. K. Sun, S. W. Chu, S. P. Tai, S. Keller, U. K. Mishra, and S. P. DenBaars, "Scanning second-harmonic/third-harmonic generation microscopy of gallium nitride," Appl. Phys. Lett. **77**, 2331–2333 (2000).
138. J. Qi, M. S. Yeganeh, I. Koltover, A. G. Yodh, and W. M. Theis, "Depletion-electric-field-induced changes in second-harmonic generation from GaAs," Phys. Rev. Lett. **71**, 633–636 (1993).
139. A. Devizis, A. Serbenta, K. Meerholz, D. Hertel, and V. Gulbinas, "Ultrafast dynamics of carrier mobility in a conjugated polymer probed at molecular and microscopic length scales," Phys. Rev. Lett. **103**, 027404 (2009).
140. O. Aktsipetrov, V. Bessonov, A. Fedyanin, and V. Val'dner, "DC-induced generation of the reflected second harmonic in silicon," JETP Lett. **89**, 58–62 (2009).